
Article:
de Carvalho, S.S., Barker, R., Folena, M.C. et al. (5 more authors) (2021) An Experimental Investigation of Top-of-Line Corrosion in a Static CO2 Environment. Corrosion, 77 (5). pp. 515-525. ISSN 0010-9312

https://doi.org/10.5006/3548

An experimental investigation of Top of Line Corrosion in a static CO_2 environment

*de Carvalho, S.S. **[‡], Barker, R.*, Folena, M.C.**, Mohammed, K.A.*, Gomes, J. A. C. P. **, Thompson, H.M. * and Neville A.**

[‡]Corresponding author. E-mail: sheylasantana@hotmail.com.

LabCorr, Technology Center, Block F - Room 210, Federal University of Rio de Janeiro, Av. Horácio Macedo, 2030, ZIP code 21941 - 598, Rio de Janeiro – RJ, Brazil, Phone: +55 (21) 3938-8500 Fax: (21) 2290-6626,Website: http://www.metalmat.ufrj.br.

*Institute of Functional Surfaces, School of Mechanical Engineering, University of Leeds, Leeds, LS2 9JT, **LabCorr, Federal University of Rio de Janeiro, Rio de Janeiro, Brazil.

ABSTRACT

This paper presents an experimental and theoretical investigation into water condensation and corrosion under non-corrosion product forming conditions at the top of line in a static, CO_2 environment. An experimental test cell is developed to measure droplet lifetimes, condensation rates, as well as in situ and integrated corrosion rates (using miniature electrodes and mass loss specimens, respectively), as a function of the surface and gas temperatures, when the gas flow is dominated by natural convection. Experimental results show clearly that that water condensation rate (WCR) is not very influential on corrosion rate at low surface temperatures (T_s) (particularly below 25°C) but becomes much more important at higher surface temperatures (>40°C). These findings are summarised in a new empirical correlation for TLC rate as a function of the condensation rate and surface temperature. A model for condensation at the top of the line for static, buoyancy-driven conditions is also presented and is shown to predict dropwise condensation rates accurately for a range of experimental conditions. The developed miniature electrodes for in situ electrochemical measurement are shown to provide an accurate interpretation of the transient response in general corrosion behaviour by giving real-time corrosion rates to complement the mass loss measurement.

KEY WORDS: *Electrochemical microprobe, CO_2 corrosion, polarization resistance, corrosion rate.*

1 INTRODUCTION

Top of the line corrosion (TLC) is encountered in the oil and gas industry when the environment outside the pipeline is cooler than the saturated vapour flow inside the pipe. This leads to significant condensation at the top of the line where corrosive species, such as organic acids and dissolved gases such as CO_2 and H_2S, can create a highly corrosive environment that can ultimately lead to pipeline failures, loss of production and environmental damage [1]. Since TLC occurs in stratified flow regimes, difficulties in deploying conventional corrosion inhibitors to the top of the line [2], have contributed to TLC becoming of worldwide importance for both offshore and onshore fields since its discovery in the 1960's [3].

Extensive laboratory studies and field data have identified the water condensation rate (WCR), gas temperature (T_g) and partial pressure of the corrosive gases as the main factors controlling TLC [4]. Many early studies of TLC in CO_2-dominated ('sweet') conditions have proposed that the WCR is the dominant parameter determining TLC severity [5], although there is evidence that its significance can be reduced by the presence of hydrocarbons [6]. Many investigations of sweet TLC have reported a directly proportional relationship between the WCR and TLC rates, which has been explained by the constant replenishment of condensate, preventing its saturation with respect to $FeCO_3$ and thereby preventing the formation of protective $FeCO_3$ films. The latter can be extremely influential by suppressing the general corrosion rate and through their subsequent breakdown which can lead to severe localised corrosion [7].

Many studies of $FeCO_3$ film formation in CO_2 TLC have appeared in the literature [8]. Olsen and Dugstad [9], for example, presented an early investigation into the relationship between the condensation and corrosion rates in TLC and their influence on $FeCO_3$ film formation. They concluded that increasing gas velocity leads to higher condensation and corrosion rates and that dense and protective $FeCO_3$ films form at high

temperature (T_g>70°C) and low WCR, while $FeCO_3$ films are much less likely to form at higher condensation rates. In the study by Gunaltun et al. [10] of sweet TLC in Indonesia, they reported several deep pits at the top of the line, which was also covered by a protective $FeCO_3$ layer. Vitse et al. [11] extended this study to consider the effect of CO_2 partial pressure, demonstrating that it promotes $FeCO_3$ precipitation and film formation leading to significant reductions in the corrosion rate when T_g>80°C.

Hinkson et al.'s [12] experimental study concluded that sweet TLC is mainly influenced by: (i) the amount of water present on the metal surface, which is determined by the condensation rate; and (ii) the chemical composition of the water condensate, both in terms of its corrosivity and the influence of Fe^{2+} ions created by corrosion which alter the pH and pH-dependent equilibria. They also showed that the presence of organic acids, such as acetic acid, tends to increase the general TLC rate and promote localised corrosion. Singer et al. [13] later showed that when the WCR is low there is a high tendency to reach $FeCO_3$ supersaturation, which can lead to the formation of $FeCO_3$ scale in the stagnant condensed droplets, encouraging the formation of dense protective layers. They also found that although higher WCRs prevent the formation of a stable and uniform corrosion layer.

The extensive experimental literature has been accompanied by numerous empirical, semi-empirical and mechanistic models to predict TLC rates in a range of corrosive environments [14]. The first empirical approach was developed by DeWaard et al. [15] for WCRs below an experimentally determined critical rate of 0.25 mL $m^{-2}s^{-1}$. This was succeeded by the empirical models of DeWaard & Lotz [16], a function of the gas temperature and partial pressure of CO_2, and that of Van Hunnink et al. [17] which addressed the systematic over-prediction of TLC rates by accounting for cases when $FeCO_3$ formation governs the corrosion rate. Important semi-empirical models include those of Pots & Hendriksen [18], who proposed the so-called 'super-saturation' model which accounted for the competition between scale formation rate and the condensation rate. The model of Vitse et al. [19], which combined a mechanistic model for film-wise condensation with a semi-empirical corrosion model, was later extended by Remita et al. [20] to take account for $FeCO_3$ film formation by incorporating a coverage factor into their analysis. Nyborg & Dugstad [21] developed a semi-empirical correlation for TLC rate that accounts for water condensation rate, $FeCO_3$ solubility and a super-saturation factor based on the concept that TLC is limited by the amount of Fe^{2+} that can be dissolved in the thin condensate film.

All models of TLC depend on the accurate prediction of WCR. In contrast to the film-wise assumption employed by Vitse et al. [11, 19], dropwise condensation is in fact the dominant mechanism at the top of the line(when the in increase in T_s is coupled with decrease of WCR). Zhang et al. [1] were the first to model dropwise condensation in the context of TLC as part of their mechanistic model for mixed CO_2/H_2S TLC, with or without corrosion product formation, based on the Nernst-Planck equation for the conservation of ionic species. Their model also accounted for chemistry in the condensate, together with corrosion and corrosion product production at the steel surface.

Despite the importance of the condensation rate as a guiding parameter of TLC, the inner wall temperature or surface temperature (T_s) is also likely to have a major influence on the corrosion product formation kinetics. However, this aspect of TLC seems to have received little attention. Hence, the present study is motivated by recent evidence that the surface temperature (T_s) can play as important role as T_g in TLC. For example, it has been demonstrated that increasing T_s can lead to a reduction in TLC rate due to longer droplet retention times during which the corrosion product can be formed [5, 22].

This paper presents a comprehensive experimental and theoretical investigation into condensation and corrosion phenomena for sweet TLC in a static environment restricted to the cases of non-layer forming. In this work, results from a newly developed experimental test cell are provided to model the TLC corrosion process. The test setup is able to provide information relating to the condensation rate, droplet lifetime, *in situ*

real-time corrosion rate (electrochemical from miniature electrodes) and integrated corrosion rate (mass loss measurement). The aforementioned information is collected using the developed rig for various test environments where corrosion product formation is not observed within the experiment test duration. The paper outlines the development of a theoretical model to predict water condensation rates in environments under buoyancy driven flow, which is subsequently compared against experimental data from the test cell. Finally, we demonstrate the ability of miniature electrodes to provide valuable real-time corrosion information and to define the transient corrosion response of carbon steel in TLC environments. A new empirical model as a function of surface temperature (T_s) and water condensation rate (WCR) is proposed to predict the general corrosion rates in non-corrosion product forming environments.

2 EXPERIMENTAL PROCEDURES

2.1 Experimental TLC test cell

The test setup comprises of a 2L glass cell with a customised lid integrated with a channelled matrix (Error! Reference source not found.**).** The internal matrix enables the flow of refrigerant to cool the TLC specimens to the desired temperature. The desired gas temperature (T_g) and surface temperature (T_s) were achieved by controlling the bulk liquid temperature through the hot plate and the refrigerant temperature in the cooler, respectively. A schematic diagram of the entire TLC setup is provided in **FIGURE 2**. The test rig is described in detail in a previous publication [23]. The rig is designed to facilitate the acquisition of corrosion rates using mass loss measurements and electrochemical techniques, as well as collection and analysis of the condensate to determine both the condensation rate and chemistry.

2.2 Mass loss and electrochemical test specimens – fabrication and surface preparation

The TLC rig described previously is designed to accommodate test specimens used for mass loss measurement as well as separate specimens for in situ, real time electrochemical measurements, both of which were used in this study. All test specimens were machined from a stock bar of X65 carbon steel. The chemical composition of the steel is provided in **TABLE 1**, with the optical microscope image in Error! Reference source not found. indicating that the material has a ferritic-pearlitic microstructure.

Mass loss test specimens (used for gravimetric analysis) were coupons (10 mm in diameter and 6 mm in thickness) with an exposed area of 0.785 cm^2 to the vapour phase. For every experiment, three test samples in total were flush-mounted into the lid of the TLC cell (the lid is made of PTFE). Tapped holes were created in the back of mass loss specimens (shown in **FIGURE 4**) enabling M5 threaded carbon steel bars to be attached to each specimen so they could easily be flush mounted into the test cell lid. Once the threaded bars were attached to the test specimens, they were fed up through the test cell lid and held in place with a lock nut to ensure each test specimen was secure in the custom lid. Prior to each experiment, all mass loss specimens were wet ground using 1200 silicon carbide (SiC), followed by rinsing with ethanol before drying with compressed air and weighing prior to insertion into the test cell lid. In addition, k-type thermocouple probes (accurate to ±0.1^oC) were placed in direct contact with specific test specimens in order to directly measure T_s (as shown in **FIGURE 4**). Neither mass loss nor electrochemical measurements were recorded from samples in instances where the thermocouple was used to measure surface T_s. Additional probes were also placed in the vapour phase of the system to measure T_g.

The miniature electrochemical probe consisted of three solid electrodes. Each electrode was fitted into samples with the same geometry as the mass loss test specimens, thus ensuring comparable surface temperatures between the different configurations (as shown in **FIGURE 4).** The working electrode consisted of a 1 mm diameter API 5L X65 steel pin, while the reference and counter were manufactured from a 1 mm diameter

Hastelloy wire. All three electrodes were positioned into a hole drilled into the mass loss specimen and isolated from one another using epoxy resin. Prior to use, the electrode three-electrode configuration was wet ground with 1200 silicon carbide (SiC) grit paper, rinsed with acetone and distilled water, and then dried. The probe was then inserted into the system by feeding the wires up through the top of the lid, before mounting the specimen against the inside of the lid and securing the wires in place using a small clamp. In specific tests, a thermocouple probe was also placed laterally across to the working electrode, touching its exposed surface to measure T_s. It is important to note that consistent measurements were recorded for both electrochemical and mass loss specimen configurations.

Depending upon the nature of the experiments, the miniature electrodes, mass loss specimens, or a combination of both were flush mounted into the three holder slots within the internal surface of the lid. In the case of the miniature electrodes, these were also connected to a potentiostat for electrochemical measurements which are described later.

2.3 Solution preparation

A CO_2-saturated 3.5 wt.% NaCl solution was used in all experiments. The solution was saturated with CO_2 for 12 h prior to each experiment to minimize dissolved oxygen in the brine. Saturation was initially performed in the glass vessel with a separate lid prior to start each experiment. The bulk solution was then heated to the desired temperature (using a hotplate) before exchanged the initial common lid for the special TLC lid with the samples assembled. CO_2 was continuously bubbled into the cell during this exchange process to preserve saturation and avoid O_2 contamination. All tests were conducted at room pressure.

Various combinations of gas, inner surface and bulk fluid temperatures were assessed within this study. Such combinations were achieved by adjusting either the cooling matrix fluid temperature (regulated by the chiller), or the bulk fluid temperature (regulated by the hot plate). The chosen conditions were pre-determined based on extensive previous temperature profiling studies.

2.4 Corrosion rate measurement (mass loss and electrochemical)

TLC corrosion rates were determined using gravimetric analysis. The prepared samples were wet-ground and cleaned before being weighed using an electronic balance to within an accuracy of 0.01 mg (producing a mass referred to as *'m_1'*). After each experiment, specimens were removed, rinsed with distilled water and acetone and dried using compressed air. Corrosion products (if present) were dissolved using Clarke's solution (an inhibited acid prepared using ASTM standard G1-03) [24]. Specimens were then re-weighed to determine their final mass (*'m_2'*). The average corrosion rate of the steel specimen was then calculated using **Equation (1)**:

$$V_{ML} = \frac{87600\,(m_1 - m_2)}{\rho_{Fe} A t} \qquad \textbf{Equation (1)}$$

where VML is the corrosion rate from mass loss in mm/year, (m1-m2) is the difference in mass (in grams) of the carbon steel specimen before the test (m1) and after removing any attached corrosion products with Clarke's solution after the experiment (m2), ρFe is the density of the carbon steel specimen (7.85 g/cm3), t is the experiment duration in hours and A is the surface area of the carbon steel specimen in cm2.

Electrochemical measurements were conducted using the three solid state probes connected to a computer-controlled ACM Gill 8 potentiostat. Three electrochemical techniques were implemented as part of this study: linear polarization resistance (LPR), electrochemical impedance spectroscopy (EIS) and Tafel polarisation. The LPR and EIS methods were utilised to quantify the corrosion rate of the X65 carbon steel

specimens. The implementation of EIS was conducted solely to determine the value of R_s and its evolution with time, allowing improved accuracy when correcting the polarisation resistances, and the data R_s can be found at previous our work [23]. LPR measurements were performed by polarising the API 5LX65 sample ±20 mV vs the Open Circuit Potential (OCP) at a scan rate of 0.25 mV/s to obtain a polarization resistance, R_p (in $\Omega.cm^2$). These measurements were performed every 5 minutes. The solution resistance, R_s (in $\Omega.cm^2$), was quantified over the course of the experiment using EIS. This was achieved by polarising the working electrode ±5 mV vs the OCP using a frequency range from 20 kHz to 0.1 Hz. R_s was subsequently subtracted from R_p to compensate for solution resistivity. The corrected polarization resistance was ultimately used to determine the corrosion rate transient response. In some instances, the value of R_s changed with time as the chemistry/volume in the condensate changed, demonstrating the importance of its continuous measurement.

Tafel polarisation curves were collected using the three-electrode cell by performing individual anodic and cathodic sweeps, starting at OCP and scanning to either approximately -400 mV and +150 mV vs. OCP at a scan rate of 0.5 mV/s. Anodic and cathodic scans were performed separately on different working electrodes for each experiment. The Tafel plots facilitated determination of the anodic (β_a) and cathodic (β_c) Tafel constants in mV/decade through measurement of their respective gradients over regions where linearity was observed between the applied voltage and the log of the measured current. The βa and βc coefficients were measured for each experiment and used those in the following equations. The Tafel slope measurements were used in **Equation (2) and Equation (3)** to determine the Stern-Geary coefficient (B), and the corrosion current density (i_{corr}), respectively.

$$B = \frac{\beta_a \beta_c}{2.303(\beta_a + \beta_c)} \qquad \textbf{Equation (2)}$$

$$i_{corr} = \frac{B}{R_p} \qquad \textbf{Equation (3)}$$

The i_{corr} value (in mA/cm^2) obtained through **Equation (3)** was then used in combination with **Equation (4)** (based on Faraday's Law) and the measured values of R_p (in $\Omega \cdot cm^2$) to determine the corrosion rate in mm/year:

$$V_E = \frac{K\, i_{corr}\, M_{Fe}}{nF\rho} \qquad \textbf{Equation (4)}$$

where K is a conversion factor to obtain corrosion rate (V_E) in units of mm/year (K = 3.16x105), M_{Fe} is the molar mass of iron (55.8 g), n is the number of electrons free in the corrosion reaction (2 electrons), ρ is the density of steel (7.87 g/cm^3) and F is the Faraday constant (96,485 coulomb/mole). All experiments were repeated at least twice, but typically in triplicate to ensure reliable and accurate results.

2.5 Condensation rate measurements

The condensate was collected via lateral channels on the inner surface of the lid which diverted the fluid. This enabled quantification of the condensation rate as a function of time. All test specimens were positioned horizontally in every test. The water condensation rate (WCR) for the entire inner surface was assumed to be uniform and was determined through regular analysis using **Equation (5)**:

$$WCR = \frac{V_w}{L_s t_c} \qquad \textbf{Equation (5)}$$

Where: WCR is the condensation rate in mL $m^{-2}s^{-1}$, V_w is the volume of condensed water in mL, t_c is the duration over which the condensed liquid is collected in s, and L_s is the internal area of the lid surface exposed to the test environment in m^2 . A range of experimental conditions were considered to determine the capabilities of the three-electrode setup. The entire experimental matrix for this study is provided in **TABLE 2**.

For static gas flow conditions, droplets at the top of line eventually detach due to gravity, when the weight of the droplet overcomes the forces due to buoyancy and surface tension. A critical condition just before the droplet falls [1], give the maximum droplet radius when the weight of droplet minus buoyancy due to gas density equal the surface tension force on hemispherical droplet. Net force on droplet downwards is equal weight of droplet minus the weight of gas, which is equal the surface tension force upwards and equal to the perimeter of hemispherical droplet x surface tension. Hence, the maximum droplet radius before it detaches from the top of the line is given by **Equation (6)**:

$$r_{\max} = \sqrt{\frac{3\sigma}{(\rho_l - \rho_g)g}} \qquad \textbf{Equation (6)}$$

Where r_{max} is maximum droplet radius, σ is the surface force on hemispherical droplet, ρ_l is the liquid density and ρ_g is the gas density.

Heat transfer in this case is dominated by natural convection. For such cases, the Nusselt number correlation due to Dittus-Boelter [25] for pipe flow can be replaced by the correlation for natural convection in **Equation (7)**:

$$\mathbf{Nu} = \mathbf{0.54(Gr\,Pr)^{0.25}} \quad \textbf{for } \left(10^5 < \mathbf{Gr\,Pr} < 10^7\right) \qquad \textbf{Equation (7)}$$

where $Gr = (d^2 \rho_{wv}^2 \beta g \Delta T)/(\mu g^2)$ and $Pr = (c_p \mu_g/k_g)$. β is the gas expansivity (K^{-1}), g is the acceleration due to gravity (m s^{-2}), $\Delta T = T_{wv} - T_s$ and μg is the gas viscosity (Pa s). This enables the heat transfer coefficient from the gas phase to be estimated by $h_g = (Nu\, k_g/d)$ in terms of the thermal conductivity of the gas phase kg (W $m^{-1} K^{-1}$) and pipe diameter d (m).

2.6 Experimental condensation rates

WCR was measured at gas temperatures 40°C ≤ T_g ≤ 70°C while the steel surface temperature, T_s, was controlled to lie within the range 8°C ≤ T_s ≤ 60°C. **TABLE 2** summarises the entire series of experiments performed with (20 h) average mass loss corrosion rates recorded. With regards to condensate measurement, the rates recorded from this study were analyzed as a function of time over 20 h within the test cell. The values of WCR were found to be stable as a function of time, with a maximum variation throughout the test of <8%.

The entire set of condensation rate data is plotted in **FIGURE 5**. Considering this figure, as expected the highest WCR was observed for the highest temperature difference (T_g - T_s) (at T_g = 70˚C and T_s=48˚C, the WCR was 1.07 ml/m^2s). The lowest WCR of 0.07 ml/m^2s was recorded when T_g = 40˚C and T_s = 35˚C. It is evident that the condensation rate is strongly dependent on the temperature of the gas phase. As the temperature increases, the condensation rate also increases since the humidity levels increase with gas temperature, thereby enhancing heat and mass transfer according to Nusselt's theory of condensation [26]. For the same gas temperature, the WCR decreases when T_s increases as shown in **FIGURE 5**.

3 RESULTS

3.1 Comparison of experimental condensation rates with the condensation model

The accuracy of the model for condensation in static TLC conditions **(APPENDIX A)** was assessed by firstly comparing the calculated values of the droplet lifetimes and condensation rates with corresponding experimental data using the experimental method proposed and at the methodology developed by Islam et al [27]. That was performed using a thermocouple positioned just beneath the sample surface and recording the temperature profile. Further details of this methodology can be found in their previous publication [27]. Droplet lifetime measurements were conducted over carefully selected conditions (some outside of the regions shown in **TABLE 2**) which gave rise to condensations rates spanning from ~0.1 to 1.6 mL m^{-2} s.

FIGURE 6 shows a comparison among the calculated and measured water droplet lifetimes in the current study (following the same methodology used by Islam et al [27]), with the droplet lifetimes determined experimentally by Islam et al. [27] at atmospheric pressure. The agreement between the predicted droplet lifetimes and both sets of experiments is very good.

FIGURE 7 shows how WCR increases with T_{gas} (for each specific value of external temperature (T_{ext})) for both methods (comparing experimental results with the theoretical model). A comparison between measured and predicted WCR's for static TLC conditions is presented in **FIGURE 8**. A strong agreement (correlation coefficient of 0.93) was obtained between experimental data and the theoretical model prediction.

3.2 Time dependent corrosion characteristics from electrochemical analysis

WCR and T_s were varied systematically to determine their effect on the average corrosion rate of carbon steel as a function of time over a period of 20 h.

FIGURE 9 provides examples of the corrosion rates determined using *in situ* LPR measurements over a period of 20 h. Across all experiments, either one or two distinct trends were observed in the corrosion response. Either the corrosion rate remained reasonably stable, or the corrosion rate response oscillated around an average value over the first 20 h, with a distinct periodicity in some instances (generally observed at higher surface temperatures). The responses (within **FIGURE 9**) provide a selection of results which depict both scenarios and illustrate the importance of such measurement to understand the variability in corrosion rate as a function of time, which helps to ensure that the integrated corrosion rates collected using mass loss measurements is an accurate reflection of the overall corrosion response.

An empirical model for the average general corrosion rate, as a function of WCR and T_s, was developed based on 20 sets of corrosion rate data for non-film-forming conditions over 20 h combined with the 11 sets of corrosion rate data from Mohammed et al. [28] using a similar static corrosion cell setup under conditions where no film formation was recorded within 24 h. Matlab was used to analyse and interpret the data. The experimental data covers the temperature range 8°C ≤ T_s ≤ 60°C and water condensation rates in the range 0.07 to 1.12. The correlation developed can be written as:

$$CR = 0.6457 - 0.227\dot{m} - 0.01004T_s + 0.01066T_s\dot{m} + 0.08722\dot{m}^2 + 0.0005529T_s^2 \qquad \textbf{Equation (8)}$$

where $\dot{m}$ is the WCR in ml/m²s, T_s is the inner surface temperature in °C and CR is the average top of line corrosion rate in mm/y.

FIGURE 10 indicates the surface plot produced by the correlation (on the right) and the respective mass loss results (on the left) based on the correlation was generate. The correlation provides a generally good representation for all experimental data, with a correlation coefficient of 0.92.

Based on surface analysis of mass loss samples at the end of each experiment and the corrosion rate response, each experiment was categorised as non-film-forming over the 20 hour time period of the experiments. It is recognised that, under certain conditions, the protective films may eventually form on the steel surface, but these conditions are not considered here. In some instances, the TLC environment can take significant periods (up to weeks) to stabilize [29]. For some systems the 20 h corrosion rate can increase with time due to the formation of iron carbide (Fe_3C) on the top of line. In other instances, a diminution in corrosion rate will occur in conjunction with the formation of protective corrosion products such as $FeCO_3$. In the context of this study, the focus is directed towards the early stages of corrosion in the absence of the formation of protective films and the absence of significant changes in the surface conditions of the steel surface (i.e. the formation of Fe_3C, or changes in wettability due to surface texture/roughness) which may accentuate corrosion.

4 DISCUSSION

4.1 Decoupling the effects of T_s and WCR on corrosion rate in TLC environments

One challenge when attempting to understand the role of individual parameters on the corrosion rate of carbon steel in TLC systems is the isolation of one individual parameter in order to study its specific role on the material dissolution characteristics. To be more specific, it is difficult to retain the WCR when changing T_s for a TLC system. The proposed empirical model permits to make comparison between different conditions difficult, and/or ambiguous in some instances.

4.1.1 Effect of WCR on average corrosion rate

Error! Reference source not found. examines the inter-relationships between T_s and WCR and the corrosion rate by the proposed model. Since the rate of renewal of the water droplets is faster at a higher WCR, the corrosion rate is expected to increase significantly with the WCR. However, at low T_s (25°C), an increase in WCR from 0.1 to 1.1 ml/m^{2}s does not dramatically affect the corrosion rate (0.75 to 0.89 mm/year), despite an increase in condensation rate by an order of magnitude.

As surface temperature reaches and exceeds 40°C in Error! Reference source not found. , an increase in corrosion rate is observed in conjunction with the rise in WCR. At T_s = 40^{o}C and 55^{o}C, an increase in WCR increases the corrosion rate from 1.1 to 1.5 and 1.8 to 2.3 mm/year, respectively.

This data suggests that if the steel temperature is sufficiently small, the extent of corrosion depends mainly on the steel temperature and is relatively insensitive to the WCR. The results presented here agree strongly with the observations of Islam et al. [27] who reported that WCR only begins to play a critical role in the TLC process when T_s exceeds 30^{o}C.

4.1.2 Effect of surface temperature on average corrosion rate

FIGURE 12 uses the empirical correlation to explore the effect of T_s in greater detail. It shows that the corrosion rate increases with T_s through an almost exponential dependence, as would be expected in non-film forming conditions.

In some situations, the effect of T_s supresses the effect of WCR, for example, observing a low WCR of 0.1 ml/m^{2}s, the average corrosion rate increased from 0.6 to 1.8 mm/year when the surface temperature increased from 10°C to 55°C. At WCR around 1.1 ml/m^{2}s, increasing surface temperature from 10°C to 55°C leads to an increase of the average corrosion rate from 0.6 to 2.26 mm/year.

Note that as T_s increases further then conditions will be more favourable for $FeCO_3$ formation, which can lead to significant reductions in corrosion rate, [8]. It is important to note that the long-term effect of exposure, specifically at high T_s and low WCR on corrosion rate is not considered here but is likely to be significantly lower based on longer term studies of other authors [27].

6 CONCLUSIONS

- Most previous studies of TLC have assumed that their behavior is controlled mainly by T_g and WCR, with the dependence on T_s mainly resulting from the dependence of the condensation process on the temperature difference (T_g-T_s). The experiments carried out here have shown that for non-film-forming conditions, T_s is an important parameter in its own right and that the same WCR at very different surface temperatures can result in very different corrosion rates.

- The experimental results, summarized in the new empirical correlation, shows clearly that WCR is not very influential on corrosion rate at low surface temperatures (particularly below 25^{o}C) but that WCR is much more important at higher surface temperatures (>40^{o}C).

- This study has also demonstrated that by using an appropriate correlation for heat transfer in buoyancy-driven flows, the condensation modelling approach developed by Zhang et al. [1], for pipe flow conditions, can predict droplet lifetimes and condensation rates under static TLC conditions.

- Furthermore, it has been demonstrated that the use of the linear polarisation test technique in conjunction with miniature electrodes provides an accurate interpretation of the general corrosion behavior. This can assist in ensuring that the corrosivity of the system is not misinterpreted when accentuation or a diminution in corrosion rate occurs with time as a result of the formation of corrosion products or other changes in the surface condition and/or texture.

5 ACKNOWLEDGMENTS

Research of this project is supported by Shell and CNPq. The authors acknowledge for their financial support and permission to present the results.

6 REFERENCES

1. Zhang, Z., et al., A mechanistic model of top-of-the-line corrosion. Corrosion, 2007. 63(11): p. 1051-1062, 2007.
2. Belarbi, Z., et al., Thiols as Volatile Corrosion inhibitors for top-of-the-line corrosion. Corrosion, 73(7),p. 892-899, 2017.
3. Mansoori, H., et al., Altering CP criteria part of unified anti-SCC approach. Oil & Gas Journal, 111(12): p. 88-88, 2013.
4. Hinkson, D., et al., Chemical composition and corrosiveness of the condensate in top-of-the-line corrosion. Corrosion, 66, p. 1-8, 2010.
5. Asher, S.L., et al., Top of the line corrosion prediction in wet gas pipelines, Corrosion 2012, NACE-2012-1303, 2012.

6. Pojtanabuntoeng, T., Singer, M., Nesic, S. Top-of-the-line corrosion in the presence of hydrocarbon co-condensation in flowing conditions, Corrosion 2012, NACE-2012-1534, 2012.
7. Barker, R., Hua, Y., Neville, A., Internal corrosion of carbon steel pipelines for dense-phase CO_2 transport in carbon capture and storage (CCS) – a review, International Materials Reviews, 62(1), p. 1-31, 2017.
8. Barker, R., et al., A review of iron carbonate ($FeCO_3$) formation in the oil and gas industry, Corrosion Science, 142, p. 312-341, 2018.
9. Olsen, S. and Dugstad, A., Corrosion under dewing conditions. Corrosion 91/472, NACE, Houston, TX, 1991.
10. Gunaltun, Y.M. and Belghazi, A., Control of top of the line corrosion in multiphase gas lines: a cast history, NACE International, NACE-99036, 1999.
11. Vitse, F., Experimental and theoretical study of the phenomena of corrosion by carbon dioxide under dewing conditions at the top of a horizontal pipeline in the presence of non-condensable gas. PhD thesis, Ohio University, 2002.
12. Hinkson, D., et al., A study of the chemical composition and corrosivity of the condensate in top of the line corrosion, Corrosion 2008, NACE-08466, 2008.
13. Singer, M., et al., Experimental study of sour top-of-the-line corrosion using a novel experimental setup. Corrosion, 69(6): 624-638, 2013.
14. Gunaltun, Y., et al., Progress in the prediction of top of the line corrosion and challenges to predict corrosion rates measured in gas pipelines, Corrosion 2010, NACE-10093, 2010.
15. De Waard, C., U. Lotz, and D. Milliams, Predictive model for CO_2 corrosion engineering in wet natural gas pipelines. Corrosion, 1991. 47(12): p. 976-985.
16. DeWaard, C., Lotz, U., Prediction of CO_2 corrosion of carbon steel, Corrosion 93, NACE paper 69, 1993.
17. Van Hunnik, E.W.J., et al., The Formation of Protective $FeCO_3$ Corrosion Product Layers in CO_2 Corrosion. Corrosion 96, NACE paper 6, 1996.
18. Pots, B.F. and Hendriksen, E., CO_2 corrosion under scaling conditions-the special case of top of line corrosion in wet gas pipelines. Corrosion 2000. NACE-00031, 2000.
19. Vitse, F., et al., Mechanistic model for the prediction of top-of-the-line corrosion risk, Corrosion, 59(12), p. 1075-1084, 2003.
20. Remita, E. et al., A kinetic model for CO_2 corrosion of steel in confined aqueous environments. J. Electrochemical Society, 155(1), C41-C45, 2008.
21. Nyborg, R. and Dugstad, A., Top of line corrosion and water condensation rates in wet gas pipelines. in Corrosion 2007, NACE-07555, 2007.
22. Qin, H. et al., Top of the line corrosion under low temperature and high condensation rate conditions. Corrosion 2011, NACE-11328, 2011.
23. de Carvalho, S. S., et al., Development and evaluation of miniature electrodes for electrochemical measurements in a CO_2 top of line corrosion environment. Corrosion Engineering, Science and Technology, p. 1-9, 2019.
24. ASTM G1-03, “Standard Practice for Preparing, Cleaning and Evaluating Corrosion Test Specimens”, ASTM International, West Conshohocken, PA, DOI: 10.1520/G0001-03R11, 2012.
25. McCabe, W.L. and Harriott, J.S., P Unit Operations of Chemical Engineering Vol. 5th ed. 1993: McGraw-Hill, Inc.
26. Stephan, K. and Green, C.V., Heat transfer in condensation and boiling. 1992: Springer.
27. Islam, M. M., Pojtanabuntoeng, T., and Gubner, R., Condensation corrosion of carbon steel at low to moderate surface temperature and iron carbonate precipitation kinetics, Corrosion Science, 111, p. 139-150, 2016.
28. Mohammed, K.A., Experimental and theoretical investigation of top of the line corrosion in CO_2 gas and oil environments, PhD thesis, University of Leeds, 2018.
29. Kaewpradap, U., et al., Top of the line corrosion-Comparison of model predictions with field data. Corrosion 2012, NACE-2012-1449, 2012.
30. Rose, J. and Glicksman, L., Dropwise condensation—the distribution of drop sizes. International Journal of Heat and Mass Transfer, 1973. 16(2): p. 411-425.

31. Graham, C. and Griffith, P., Drop size distributions and heat transfer in dropwise condensation. International Journal of Heat and Mass Transfer, 1973. 16(2): p. 337-346.

APPENDIX A: CONDENSATION MODEL FOR STATIC TLC CONDITIONS

The following model is an adaptation of Zhang et al [1] work to static conditions generally used at laboratory tests.

Since condensation at the top of the line is based on dropwise condensation, a distribution of droplets between a minimum radius, r_{min}, and a maximum radius, r_{max}, is assumed equal **Equation (A.1)** [30]:

$$N(r) = \frac{n}{\pi r^2 r_{max}} \left(\frac{r}{r_{max}}\right)^{n-1} \quad \textbf{Equation (A.1)}$$

where n=1/3. The total heat flux, Q_T (W/m^2), is given by **Equation (A.2)**:

$$Q_T = h_g\left(T_b^g - T_i^g\right) + \dot{m} H_{fg} \quad \textbf{Equation (A.2)}$$

where h_g is the heat transfer coefficient from the gas (W/m^{2}K), T_b^g and T_i^g are the bulk gas and gas/droplet interface temperatures (K), $\dot{m}$ is the condensation rate (kg/m^{2}s) and H_{fg} is the latent heat of condensation of water vapour (J/kg). The total heat flux can be re-written in terms of the following expression in **Equation (A.3):**

$$Q_T = \int_{r_{min}}^{r_{max}} \frac{\left(T_i^g\left(1-\frac{2\sigma}{H_{fg}\, r\, \rho_{wv}}\right) - T_o^w\right) N(r)dr}{\left(\frac{1}{4\pi r k_{H_2O}} + \frac{1}{2\pi r^2 h_i} + \frac{d_w}{4\pi r^2 k_w}\right)} = A T_i^g - B T_o^w \quad \textbf{Equation (A.3)}$$

where σ is the surface tension of water (N/m), ρ_{wv} is the density of the water vapour (kg/m^3), T_o^w is the outer wall temperature (K), k_{H_2O} is the thermal conductivity of water (W/mK), h_i is the heat transfer coefficient at the droplet interface (W/m^{2}K), d_w is the thickness of the pipe (m) and k_w is the thermal conductivity of the steel pipe (W/mK). The constants A and B are given by **Equation A.4** and **A.5**, respectively:

$$A = \int_{r_{min}}^{r_{max}} \frac{\left(\left(1-\frac{2\sigma}{H_{fg}\, r\, \rho_{wv}}\right)\right) N(r)dr}{\left(\frac{1}{4\pi r k_{H_2O}} + \frac{1}{2\pi r^2 h_i} + \frac{d_w}{4\pi r^2 k_w}\right)} \quad \textbf{Equation (A.4)}$$

$$B = \int_{r_{min}}^{r_{max}} \frac{N(r)dr}{\left(\frac{1}{4\pi r k_{H_2O}} + \frac{1}{2\pi r^2 h_i} + \frac{d_w}{4\pi r^2 k_w}\right)} \quad \textbf{Equation (A.5)}$$

The condensation rate $\dot{m}$ can also be written in the form given by **Equation (A.6)**:

$$\dot{m} = \frac{h_g}{C_p} Le^{\frac{2}{3}} \left(\frac{P_{sat}(T_b^g) - P_{sat}(T_i^g)}{P_{tot}}\right) \frac{M_{water}}{M_{gas}} \quad \textbf{Equation (A.6)}$$

where c_p is the heat capacity of the gas (J/kgK), *Le* is the Lewis number of water vapour, P_{sat} is the saturated water vapour pressure (bar) at temperature T (in ˚C) given by **Equation (A.7)**:

$$\boldsymbol{P_{sat}(T) = \frac{10^{(A_1 - B_1/(C_1+T))}}{750}} \qquad \textbf{Equation (A.7)}$$

A_1=8.07131, B_1=1730.63, C_1=233.426, P_{tot} is the total gas pressure (bar), M_{water} is the molecular weight of water (g/mol) and M_{gas} is the mean molecular weight of the gas (g/mol). Equating the two expressions for ṁ leads to the following **Equation (A.8)** for T_i^g:

$$\boldsymbol{h_g T_b^g + H_{fg} \frac{h_g Le^{2/3}}{C_p} \frac{P_{sat}(T_b^g)}{P_{tot}} \frac{M_{water}}{M_{gas}} + BT_0^w = h_g T_i^g + AT_i^g + H_{fg} \frac{h_g Le^{2/3}}{C_p} \frac{P_{sat}(T_i^g)}{P_{tot}} \frac{M_{water}}{M_{gas}}} \qquad \textbf{Equation (A.8)}$$

Maximum and Minimum Droplet Radii

The minimum droplet radius is calculated from the Clapeyron relation [31] **Equation (A.9)**:

$$\boldsymbol{r_{min} = \frac{2\,T_s \sigma}{H_{fg} \rho_{wv}\, \Delta T}} \qquad \textbf{Equation (A.9)}$$

7 FIGURES

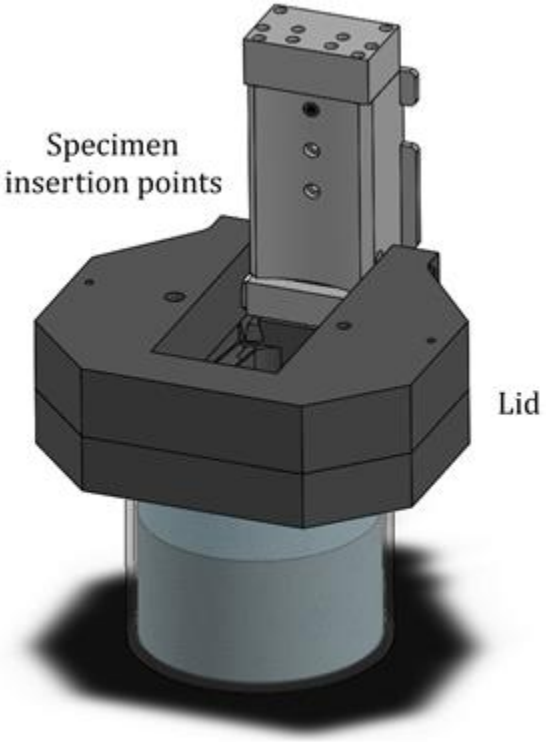

FIGURE 1. Glass cell and customized lid with cooling matrix.

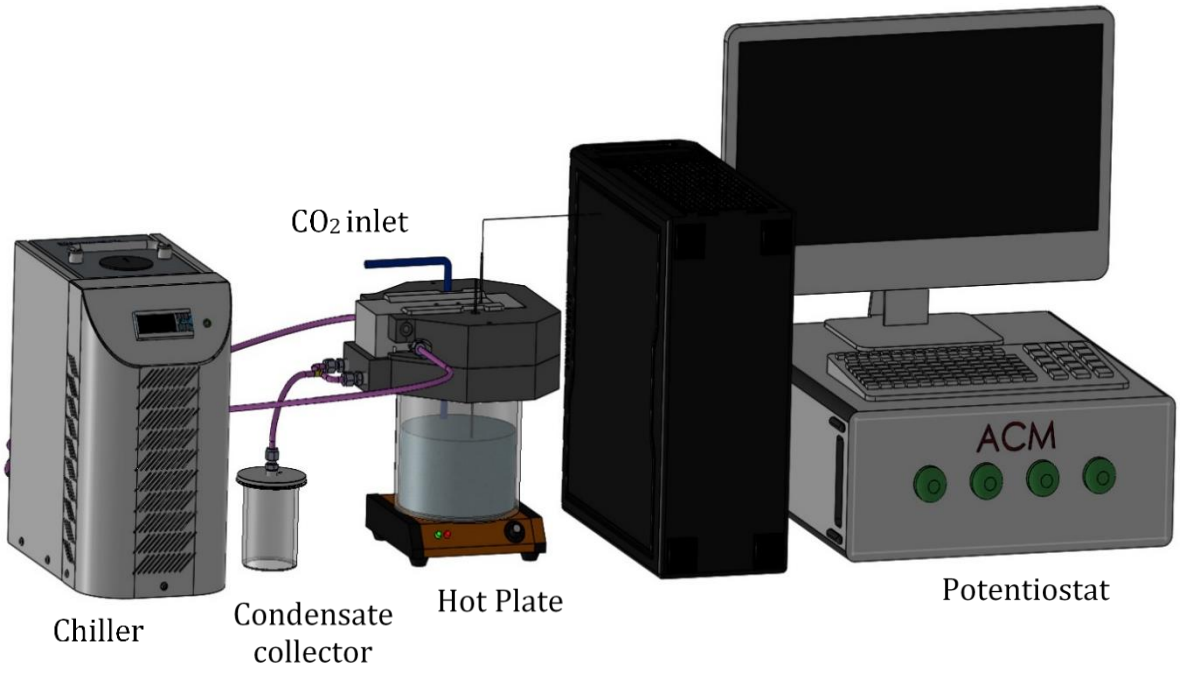

FIGURE 2. Schematic diagram of the entire TLC experimental setup.

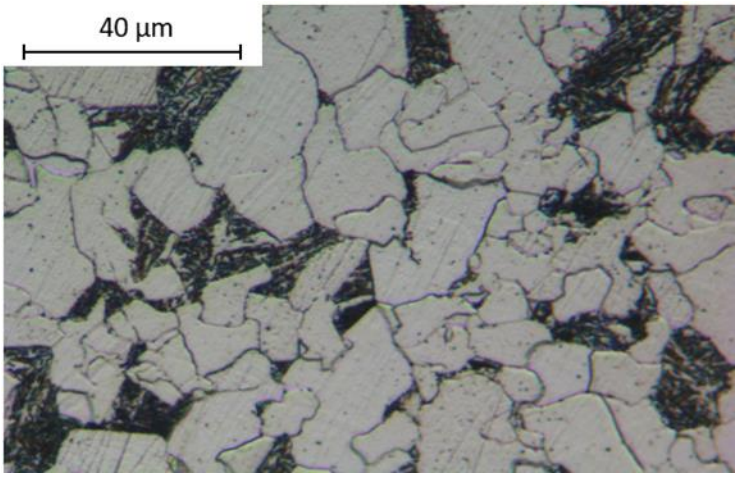

FIGURE 3. Microstructure of API 5L X65 steel indicating ferrite and pearlite microstructure.

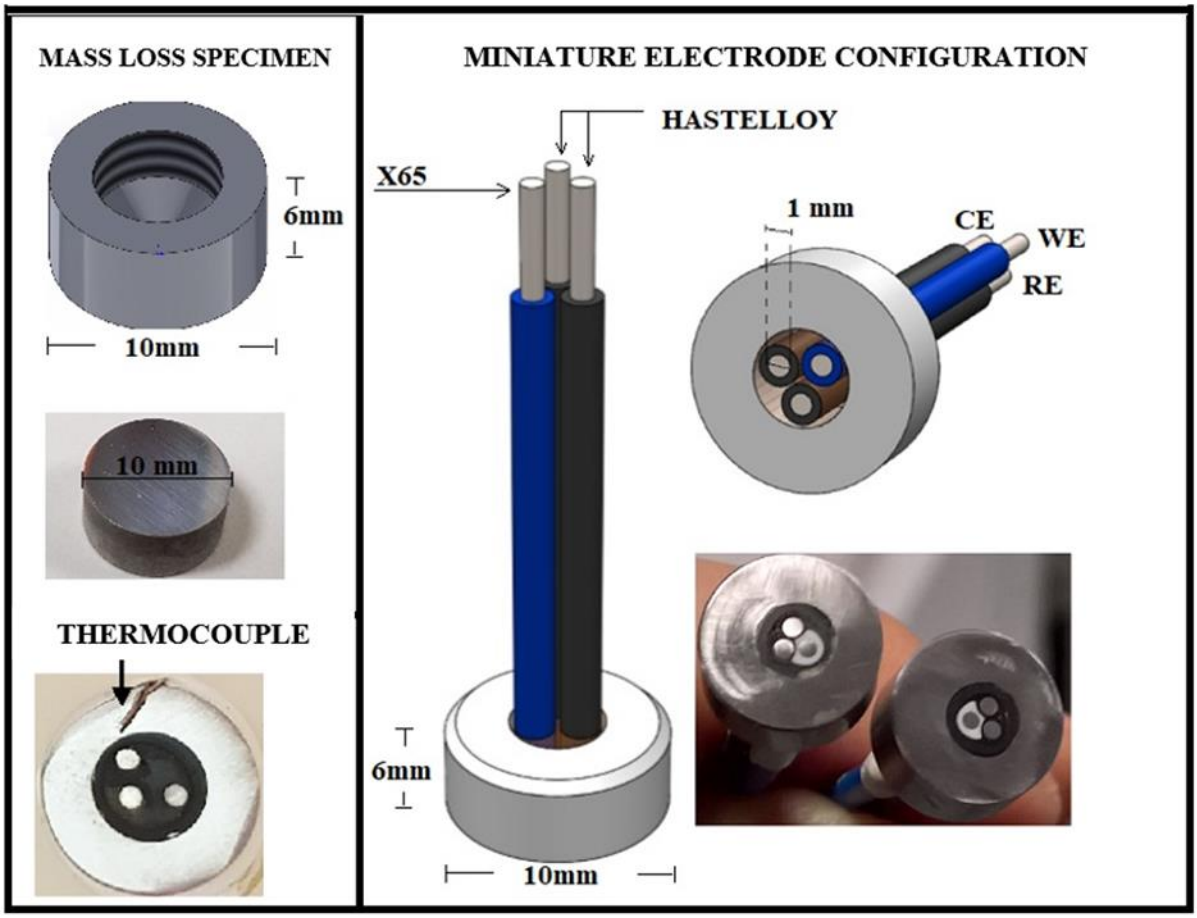

FIGURE 4. Miniature electrode configuration and mass loss specimen.

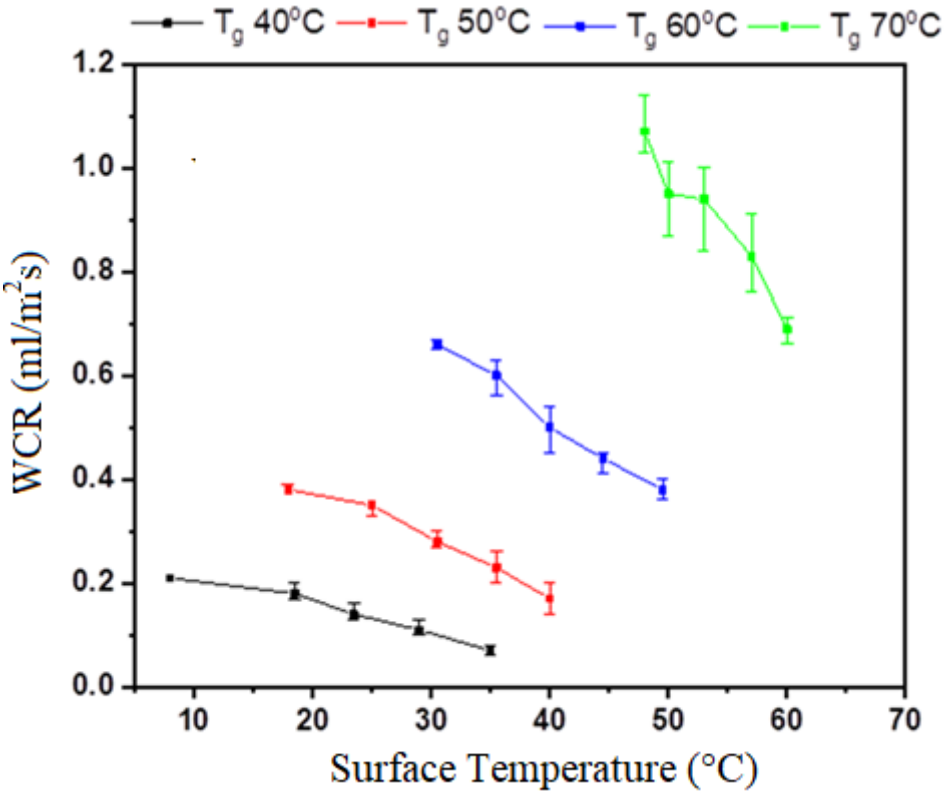

FIGURE 5. Dependence of condensation rate, WCR, on T_s for different gas temperatures, T_g.

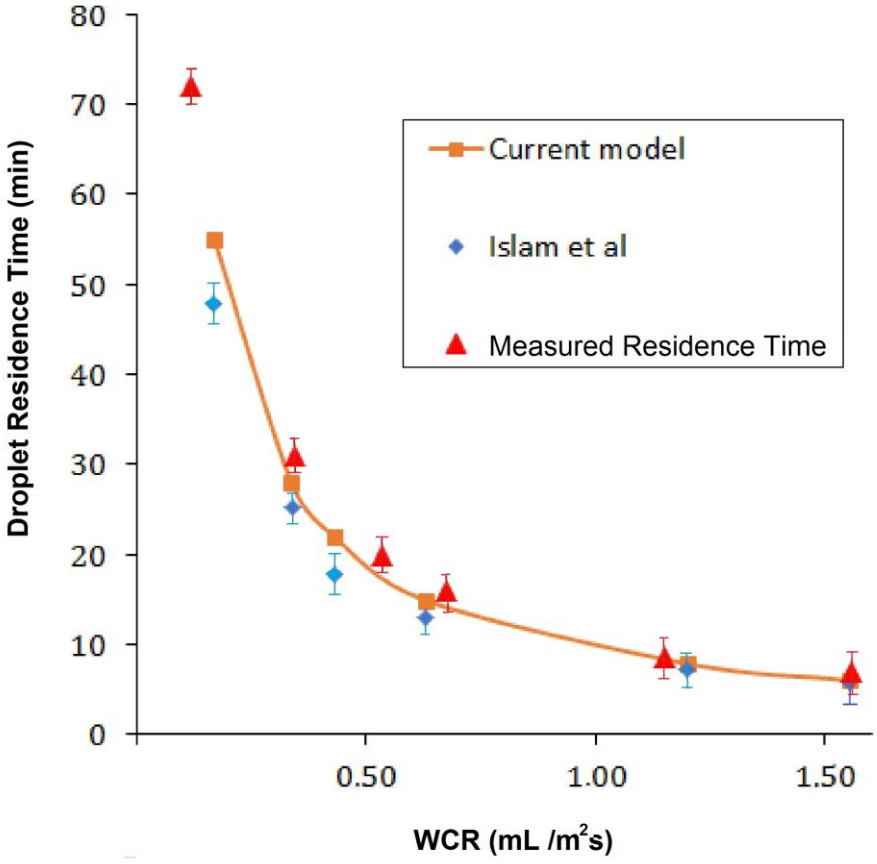

FIGURE 6. Comparison between predicted and experimental droplet lifetimes in the current study and the experiments of Islam et al. [27].

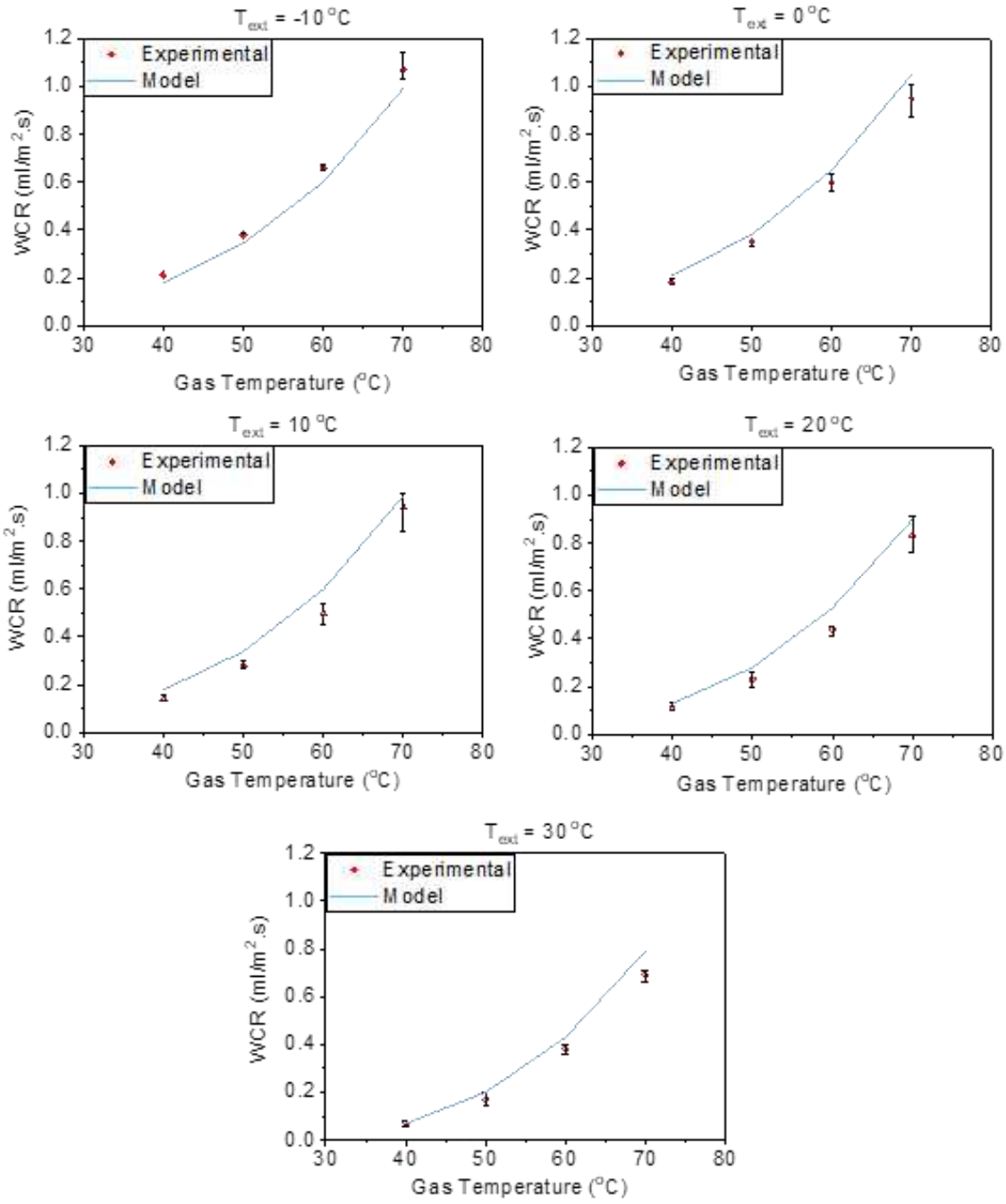

0

FIGURE 7. Comparison between experimentally measured and predicted condensation rates for external temperature Text = -10°C, 0°C, 10°C, 20°C and 30°C, at atmospheric pressure under static TLC conditions.

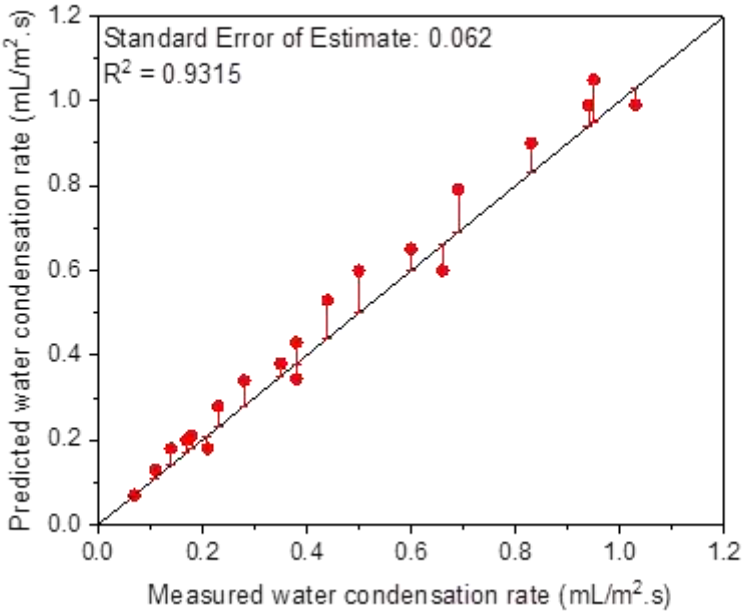

FIGURE 8. Comparison between experimental WCR data and predicted theoretical model [28].

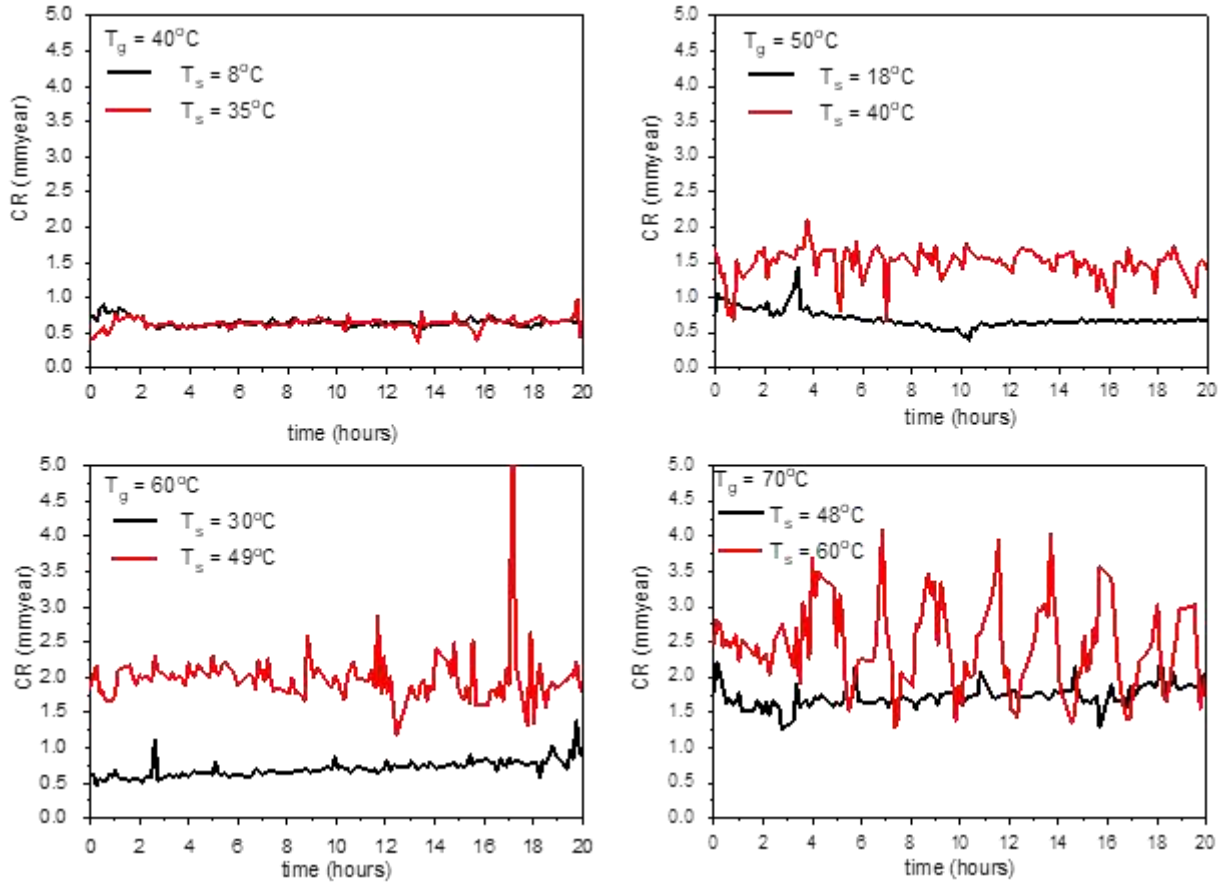

FIGURE 9. *In situ* corrosion rate by LPR at: Tg = 40°C (a), 50°C (b), 60°C (c) and 70°C (d) versus time with different surface temperatures.

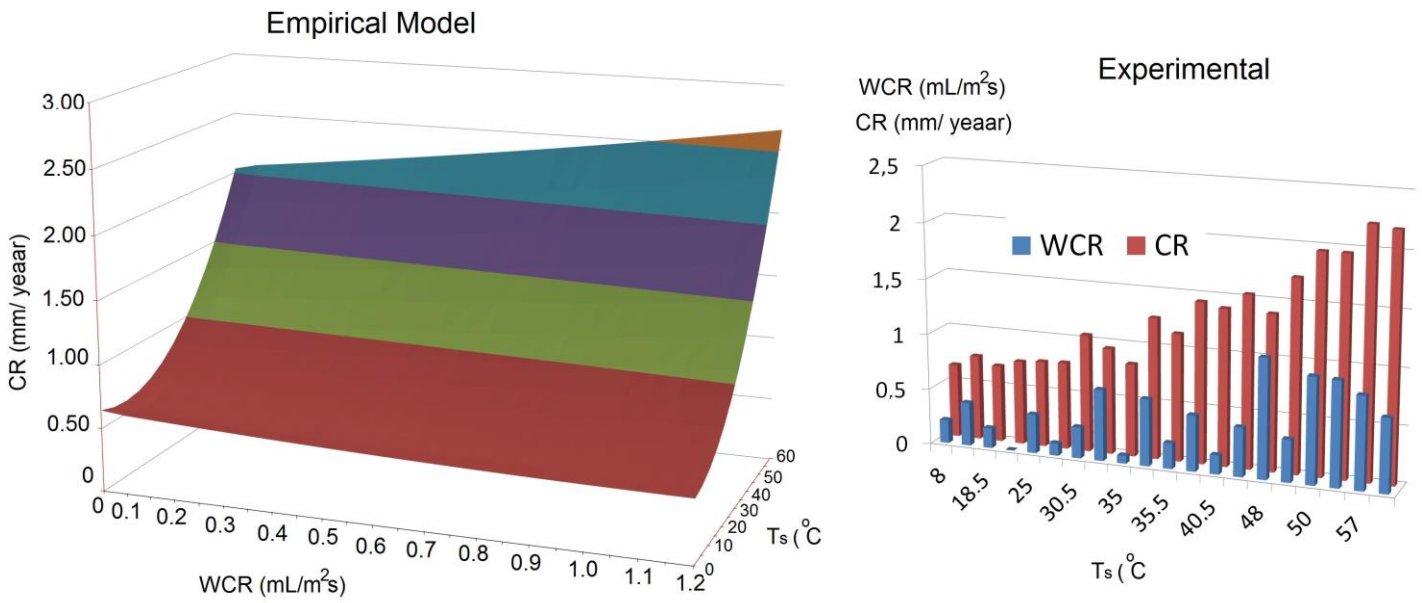

FIGURE 10. A plot of the empirical model of the combined effect of surface temperature and water condensation rate on the average general TLC rate over 20 h and the experimental weight loss results.

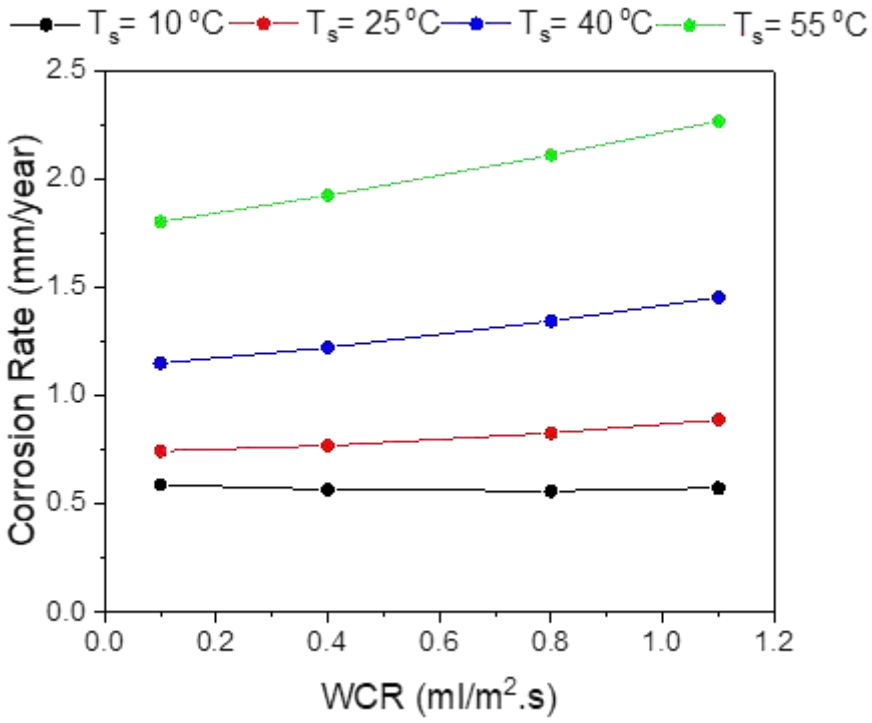

FIGURE 11. The effect of condensation rate on TLC rate predict by the model at different wall temperatures and at a total pressure of 1 bar.

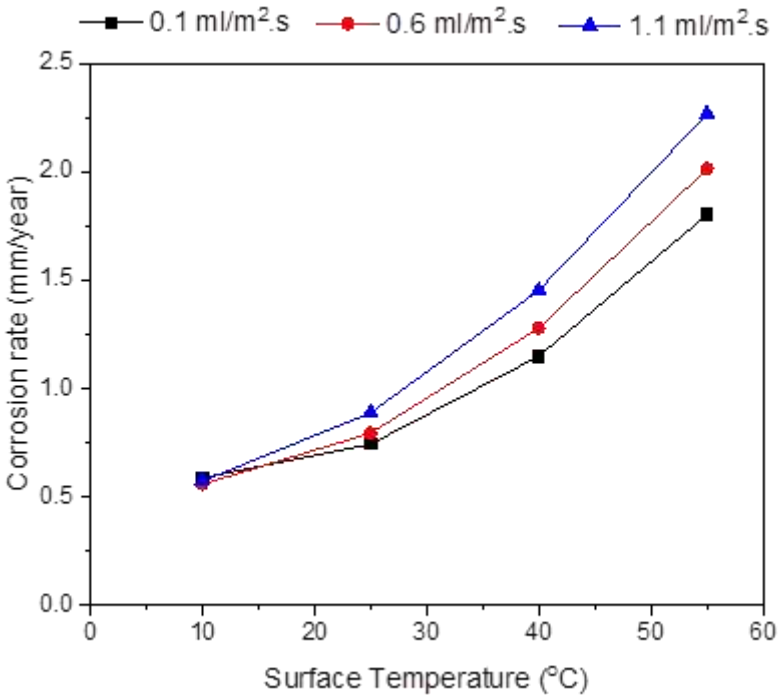

FIGURE 12. Effect of the surface temperature, T_s, on TLC rate at different water condensation rates at a total pressure of 1 bar.

8 FIGURE CAPTIONS

FIGURE 1. Glass cell and customized lid with cooling matrix.

FIGURE 2. Schematic diagram of the entire TLC experimental setup.

FIGURE 3 Microstructure of API 5L X65 steel indicating ferrite and pearlite microstructure.

FIGURE 13. Miniature electrode configuration and mass loss specimen.

FIGURE 5. Dependence of condensation rate, WCR, on Ts for different gas temperatures, Tg.

FIGURE 6. Comparison between predicted and experimental droplet lifetimes in the current study and the experiments of Islam et al. [27].

FIGURE 7. Comparison between experimentally measured and predicted condensation rates for external temperature Text = -10°C, 0°C, 10°C, 20°C and 30°C, at atmospheric pressure under static TLC conditions.

FIGURE 8. Comparison between experimental WCR data and predicted theoretical model [28].

FIGURE 9. In situ corrosion rate by LPR at: Tg = 40°C (a), 50°C (b), 60°C (c) and 70°C (d) versus time with different surface temperatures.

FIGURE 10. A plot of the empirical model of the combined effect of surface temperature and water condensation rate on the average general TLC rate over 20 h and the experimental weight loss results.

FIGURE 11. The effect of condensation rate on TLC rate predict by the model at different wall temperatures and at a total pressure of 1 bar.

FIGURE 12. Effect of the surface temperature, Ts, on TLC rate at different water condensation rates at a total pressure of 1 bar.

9 TABLES

TABLE 1. X65 carbon steel composition (wt.%), specified [23].

C	Si	Mn	P	S	Cr	Mo	Ni
0.12	0.18	1.27	0.008	0.002	0.11	0.17	0.07
Cu	**Sn**	**Al**	**B**	**Nb**	**Ti**	**V**	**Fe**
0.12	0.008	0.022	0.005	0.054	0.001	0.057	Bal

TABLE 2. After 20 hours average corrosion rate (V_{ML}) at atmospheric pressure, as well as condensation rates (WCR).

Temperature			Rate	
Gas T_g (°C)	Surface T_s (°C)	External Text (°C)	Condensation WCR (ml m^{-2} s^{-1})	Corrosion (mass loss) V_{ML} (mm y^{-1})
40 ± 0.5	8 ± 1.0	-10	0.21± 0.00	0.66 ± 0.13
50 ± 0.5	18 ± 1.5	-10	0.39 ± 0.01	0.76 ± 0.04
60 ± 0.5	30.5 ± 1.0	-10	0.64 ± 0.01	0.95 ± 0.03
70 ± 0.5	48 ± 1.0	-10	1.07 ± 0.07	1.39 ± 0.19
40 ± 0.5	18.5 ± 0.5	0	0.18 ± 0.02	0.69 ± 0.11
50 ± 0.5	25 ± 0.5	0	0.35 ± 0.02	0.77 ± 0.07
60 ± 0.5	35.5 ± 0.5	0	0.60 ± 0.04	1.26 ± 0.15
70 ± 0.5	50 ± 0.5	0	0.95 ± 0.08	1.96 ± 0.12
40 ± 0.5	23.5 ± 0.5	10	0.14 ± 0.02	0.75 ± 0.22
50 ± 0.5	30.5 ± 0.5	10	0.28 ± 0.02	1.05 ± 0.22
60 ± 0.5	40 ± 1.0	10	0.50 ± 0.02	1.44 ± 0.30
70 ± 0.5	53 ± 1.0	10	0.94 ± 0.10	1.96 ± 0.15
40 ± 0.5	29 ± 0.5	20	0.11 ± 0.02	0.78 ± 0.25
50 ± 0.5	35.5 ± 0.5	20	0.23 ± 0.03	1.14 ± 0.23
60 ± 0.5	44.5 ± 1.0	20	0.44 ± 0.03	1.54 ± 0.09
70 ± 0.5	57 ± 1.0	20	0.83 ± 0.08	2.22 ± 0.25
40 ± 0.5	35 ± 0.5	30	0.07 ± 0.01	0.83 ± 0.21
50 ± 0.5	40.5 ± 1.5	30	0.17 ± 0.03	1.40 ± 0.13
60 ± 0.5	49.5 ± 0.5	30	0.38 ± 0.02	1.72 ± 0.19
70 ± 0.5	60 ± 1.0	30	0.66 ± 0.03	2.19 ± 0.17